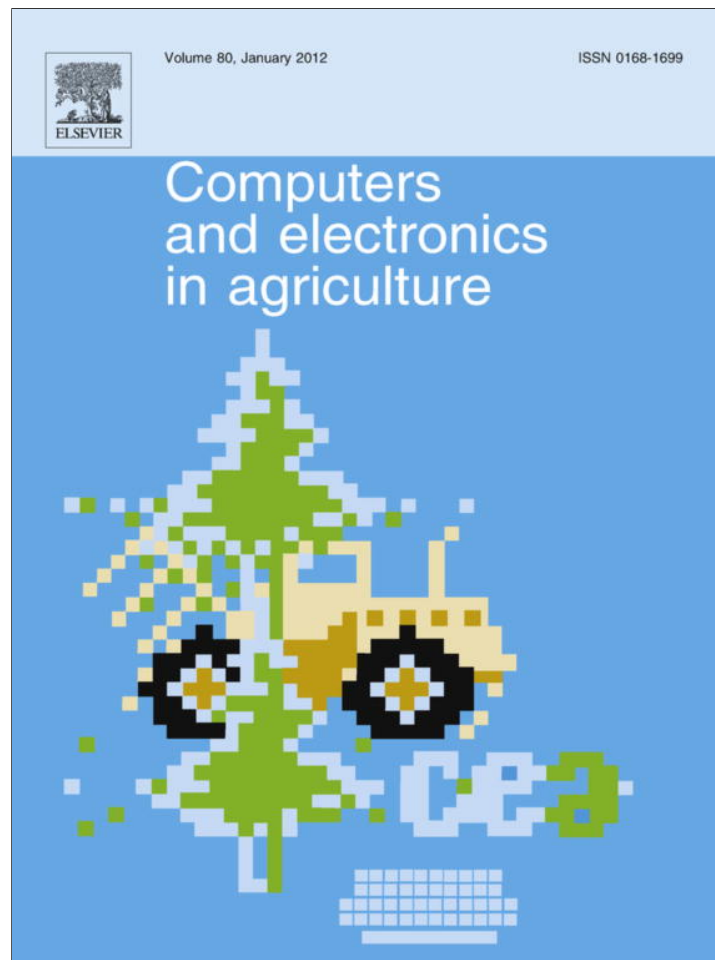


Provided for non-commercial research and education use.  
Not for reproduction, distribution or commercial use.



(This is a sample cover image for this issue. The actual cover is not yet available at this time.)

This article appeared in a journal published by Elsevier. The attached copy is furnished to the author for internal non-commercial research and education use, including for instruction at the authors institution and sharing with colleagues.

Other uses, including reproduction and distribution, or selling or licensing copies, or posting to personal, institutional or third party websites are prohibited.

In most cases authors are permitted to post their version of the article (e.g. in Word or Tex form) to their personal website or institutional repository. Authors requiring further information regarding Elsevier's archiving and manuscript policies are encouraged to visit:

<http://www.elsevier.com/copyright>



Contents lists available at SciVerse ScienceDirect

## Computers and Electronics in Agriculture

journal homepage: [www.elsevier.com/locate/compag](http://www.elsevier.com/locate/compag)

## A high-resolution airborne four-camera imaging system for agricultural remote sensing

Chenghai Yang\*

USDA-ARS Southern Plains Agricultural Research Center, 2771 F and B Road, College Station, TX 77845, USA

## ARTICLE INFO

## Article history:

Received 24 January 2012

Received in revised form 2 July 2012

Accepted 4 July 2012

## Keywords:

Airborne imaging system

CCD camera

Bandpass filter

Band-to-band alignment

Multispectral image

## ABSTRACT

This paper describes the design and testing of an airborne multispectral digital imaging system for remote sensing applications. The system consists of four high resolution charge coupled device (CCD) digital cameras and a ruggedized PC equipped with a frame grabber and image acquisition software. The cameras are sensitive in the 400 to 1000 nm spectral range and provide  $2048 \times 2048$  active pixels with 12-bit data depth. A 24 mm lens is attached to each camera via an F to C mount adapter, resulting in an imaging size of 0.63 times the flight altitude. The four cameras are equipped with blue (430–470 nm), green (530–570 nm), red (630–670 nm), and near-infrared (NIR) (810–850 nm) bandpass interference filters, respectively, but have the flexibility to change filters for desired wavelengths and bandwidths. The cameras are arranged in a quad configuration and attached to adjustable mounts that facilitate aligning the cameras horizontally, vertically, and rotationally. The image acquisition software allows the synchronized black-and-white band images from the cameras to be viewed on the computer monitor in any one of the four modes: a quad, one band image at a time, a normal color composite, or a color-infrared (CIR) composite. The band images are refreshed continuously to allow the operator to selectively save images with correct areas of interest. The selected four-band composite image is saved as a tiff file and consecutive images can be saved in 1-s intervals. A band-to-band alignment procedure based on the first- and second-order polynomial transformations was presented to further align the four band images. The system performed well in both stationary and airborne testing conditions. Airborne images obtained from agricultural fields, rangelands, and waterways demonstrate that this system has potential for monitoring crop pest conditions, mapping invasive weeds and assessing natural resources.

Published by Elsevier B.V.

## 1. Introduction

Airborne remote sensing technology has been used as a versatile data-gathering tool for monitoring crop conditions and assessing natural resources for 30 years. Development of this technology was stimulated by research and applications of multispectral video imaging systems in the 1980s (Meisner and Lindstrom, 1985; Nixon et al., 1985; Everitt et al., 1989). With advances in electronic imaging and computer technology, true digital imaging systems were developed in the 1990s (Pearson et al., 1994; Everitt et al., 1995; Escobar et al., 1997). Availability of these digital systems made airborne remote sensing even more useful and attractive for many applications. Among the advantages of airborne imaging systems are their low cost, high spatial resolution, real-time or near-real-time availability of imagery for visual assessment and computer image processing, and ability to obtain data in narrow spectral bands in the visible to mid-infrared region of the spectrum (Mausel et al., 1992; King, 1995).

Most airborne digital imaging systems can provide multispectral image data at spatial resolutions ranging from less than 1 m to a few meters and at 2–12 narrow spectral bands in the visible to near-infrared (NIR) regions of the electromagnetic spectrum. Airborne multispectral imagery has been widely used to assess within-field crop growth conditions and yield variability for precision agriculture (Moran et al., 1997; Senay et al., 1998; Yang and Anderson, 1999; Pinter et al., 2003; Inman et al., 2008).

Hyperspectral imaging systems can capture imagery from tens to hundreds of narrow spectral bands and offer new opportunities for better differentiation and estimation of biophysical attributes. Many commercial airborne hyperspectral sensors such as AVIRIS, CASI, HYDICE, HyMap, and AISA have been developed and used for various remote sensing applications. Advances in CCD cameras, frame grabber boards, and modular optical components have also led to developments of low-cost airborne hyperspectral imaging systems from off-the-shelf products (Mao, 1999; Yang et al., 2003). Despite significant progress in airborne hyperspectral remote sensing, hyperspectral imagery has not been used as widely as multispectral imagery partially due to the high costs of data acquisition and the special needs for handling and processing vast

\* Tel.: +1 979 260 9530.

E-mail address: [chenghai.yang@ars.usda.gov](mailto:chenghai.yang@ars.usda.gov)

volumes of data. Airborne hyperspectral imaging sensors employ an aircraft as a platform for pushbroom scanning. A raw hyperspectral image cube is formed by a collection of scanned lines with all the bands. Since the stability of the platform is affected by the surrounding turbulent atmosphere during image acquisition, variations in altitude, attitude, and velocity will cause geometric distortions on the hyperspectral image (Gregory et al., 1999). Although inertia measurement units (IMUs) or gyro mounts are used to dampen and measure the variations for post-corrections, the spatial coherence among the lines within each band image is compromised.

Commercial availability of high resolution satellite data provides new opportunities for remote sensing applications that require high resolution image data. The IKONOS satellite sensor captures four channels of multispectral data at 4 m resolution and the QuickBird sensor provides four channels of multispectral data at 2.4 m (at nadir) or 2.8 m (off nadir) resolution. Two recently launched satellite sensors, GeoEye-1 and WorldView 2, have further narrowed the gap in spatial resolution between satellite and airborne imagery. GeoEye-1 provides four spectral bands at 1.65 m resolution and WorldView 2 offers eight spectral bands at 1.8 m resolution. Moreover, the high revisit frequency and fast turnaround time of these satellite sensors are certainly advantages over traditional satellites. These advantages combined with their relatively large aerial coverage and ability to take imagery over any geographic area make high resolution satellite imagery even more attractive than aerial photos and airborne imagery for some applications.

Despite the availability of high resolution satellite sensors, airborne multispectral imaging systems still offer some advantages, including the immediate availability for real-time assessment and the flexibility to change filters for desired wavelengths and bandwidths. Most airborne multispectral imaging systems employ multiple CCD cameras, each of which is equipped with a different bandpass filter. This approach has the advantage that each camera can be individually adjusted for optimum focus and aperture settings, but has the disadvantage that the images from all the bands have to be properly aligned. With multiple optical systems, it is very difficult to achieve this alignment optically or mechanically, so a software-based registration procedure is commonly used to align the band images.

Another approach is to use a beam splitting prism and multiple CCD sensors built in one single camera to achieve multispectral imagery. One such system is the MS4100 multispectral 3CCD camera (Geospatial Systems, Inc., West Henrietta, NY), which uses a beam splitting prism and three CCD sensors to acquire images in 3–5 spectral bands within the 400–1100 nm spectral range. When the camera is configured to capture three bands, each CCD sensor is designated for one band. However, when four or five bands are captured, two or three visible bands will be interpolated using the Bayer filter from one of the CCD sensors. Although the camera can be configured to the specified spectral bands, it is difficult to change the bands once they are configured. It also has the alignment issue among the three CCD sensors. Lan et al. (2009) evaluated the MS4100 system with the four-band configuration for pest management. Kise et al. (2010) reported a three-band image acquisition system consisting one front lens, one cold mirror, one beam splitter and three sets of CCD cameras, back lenses and interchangeable filters. This design has the flexibility for filter change, but has the same alignment problem.

The USDA-ARS remote sensing group at Weslaco has focused considerable research effort on airborne electronic imaging systems as a tool for remote sensing applications since the 1980s. More recently, a hyperspectral imaging system described by Yang et al. (2003) was integrated with a three-band imaging systems described by (Escobar et al., 1997) for precision agriculture and pest

management (Yang et al., 2005; Yang and Everitt, 2007; Yang et al., 2009). The three-camera imaging system had the capability of obtaining 8-bit color-infrared (CIR) images with  $1024 \times 1024$  pixels. The three CCD cameras were filtered for spectral observations in the green (555–565 nm), red (625–635 nm), and NIR (845–857 nm) wavelength intervals, respectively. The system was later upgraded to enhance image acquisition speed and obtain images with  $1280 \times 1024$  pixels. The hyperspectral imaging system was configured to capture 12-bit images in 128 bands in the visible to NIR region of the spectrum (457 to 922 nm) with a bandwidth of 3.6 nm. Because of the narrow radiometric range of the multispectral system, it required that the apertures of the cameras be adjusted for different targets during image acquisition to take advantage of the full radiometric range and to avoid image saturation. Another limitation of the system was that it was configured to capture CIR imagery only. One additional camera filtered with a blue band will allow both color and CIR imagery to be captured. With four cameras, it will also allow the optimal bands identified by the hyperspectral system to be implemented for particular applications. Therefore, the objectives of this study were to: (1) develop a four-camera multispectral imaging system that will be able to capture high resolution imagery without the need to change aperture settings during image acquisition; and (2) demonstrate the potential use of the system with examples for a variety of agricultural and natural resource applications.

## 2. System design and description

### 2.1. Camera configuration

To meet research and application requirements, the new multispectral system should have the following characteristics: (1) four spectral bands in the visible to NIR region of the spectrum with the flexibility to change center wavelengths and bandwidths; (2) 12-bit data depth (0–4095 gray levels) to allow the aperture of each camera to be preset for diverse ground targets; (3) 2 k by 2 k pixel array to obtain high resolution imagery; (4) color and CIR image display for real-time assessment; and (5) fast acquisition speed to allow selected images to be captured and saved in seconds. In addition, since this system will be used with the hyperspectral imaging system, it should have slightly larger ground coverage than the hyperspectral system.

The multispectral imaging system was designed with the multiple-camera approach to meet the above criteria. Four identical CCD cameras and four sets of optical components were selected to build the system. Fig. 1 shows one camera assembly, which consists of a



Fig. 1. A high resolution CCD camera with a mount adapter, a filter and a focal lens.

**Table 1**

Major specifications of the XVM4021 CCD camera.

Sensor type	Interline CCD, progressive scan
Sensing area	15.2 mm × 15.2 mm
Pixel size	7.4 μm × 7.4 μm
Active pixels	2048 (h) × 2048 (v)
Pixel depth	12 bit
Spectral range	400–1000 nm
Frame rate	15.76 fps dual tap
Binning	Independent H&V: 1–16x
Gain control	Digital 0.001 to 16x
Pixel clock	40 MHz
Lens mount	C-mount
Dimensions	37 mm × 57 mm × 57 mm
Weight	240 g
Operating temperature	0–50 °C

XMV-4021 CCD camera (Illunis LLC, Minnetonka, MN), a Century Precision LA-NICJ Nikon F to C mount adapter (Schneider Optics, Hauppauge, NY), a bandpass interference filter attached inside the adapter (Ealing Catalog Inc., Rocklin, CA), and an AF Nikkor 24 mm f/2.8D lens (Nikon Corporation, Tokyo, Japan).

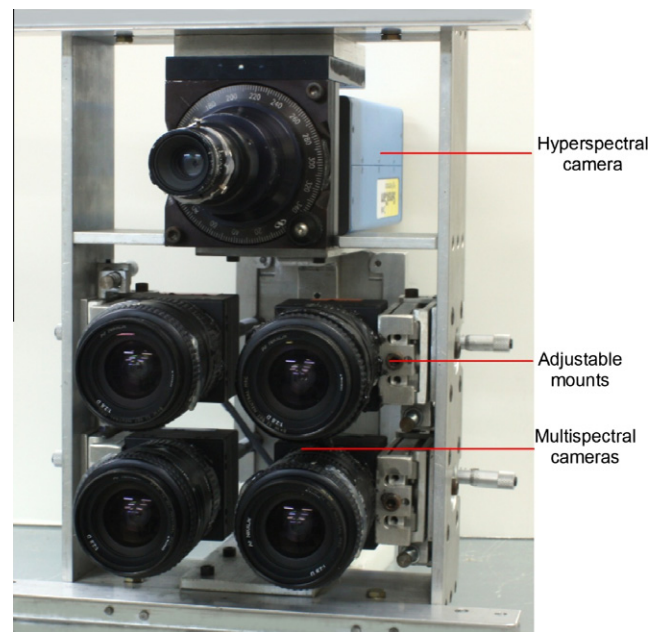
The XVM-4021 camera is a 12-bit interline CCD camera with 2048 (h) × 2048 (v) active pixels. It is sensitive in the 400–1000 nm spectral range. Table 1 gives the major specifications of the camera. The F to C mount adapter is used to connect the F-mount focal lens to the C-mount camera and is also used to house the filter. A different bandpass interference filter can be used for each camera to obtain the desired center wavelength and band widths. For the testing of the cameras, two sets of filters with a diameter of 25.4 mm were used. Both sets of filters have the same center wavelengths of 480 nm (blue), 560 nm (green), 650 nm (red), and 830 nm (NIR), but the bandwidth or the full width at half maximum (FWHM) is 10 nm for one set and 40 nm for the other. Other visible and NIR bandpass filters are also available for use for different research and application needs. The focal lens has a fixed focal length of 24 mm and an aperture scale of  $f/2.8$  to  $f/22$ .

Fig. 2 shows the configuration of the four-camera multispectral imaging system along with the hyperspectral camera. The four cameras are arranged in a quad configuration and attached to an aluminum frame via adjustable mounts, which facilitate aligning the cameras horizontally, vertically, and rotationally. This mechanical alignment will ensure the cameras to have a similar field of view and allow color and CIR composite images to be viewed on the computer display for real-time assessment.

## 2.2. Image acquisition PC and software

The digital images from the four cameras are captured by a ruggedized PC through an image frame grabber board installed in a PCI slot in the computer. The custom PC is a 2.49 GHz Intel Xeon processor-based system with a 3.24 GB RAM and a 1.4 TB hard drive. The operating system of the computer is Microsoft Windows XP and the display is a Sony SDM-S204 LCD monitor with a resolution of 1600 × 1200 pixels. The image frame grabber is a KBN-PCE-CL4-D PCI Express interface board (BitFlow, Inc., Woburn, MA), which can simultaneously acquire data from the four cameras. The cameras are connected to the PCI interface board via four Camera Link cables.

The control parameters for the camera, including trigger mode, exposure time, digital gain, and horizontal and vertical binning factors, can be set with the software provided with the camera before image acquisition. The synchronization of the four cameras and image acquisition were accomplished by the software developed by Subtechnique, Inc. (Alexandria, VA). The software allows synchronized black-and-white band images from the four cameras



**Fig. 2.** A four-camera multispectral imaging system along with a hyperspectral camera.

to be viewed on the computer monitor in any one of the four modes: a quad, one band image at a time, a normal color composite, or a CIR composite. The band images are refreshed continuously to allow the operator to selectively save images with desired areas of interest. The selected four-band composite is captured instantaneously when the save button is pushed and then saved as a tiff file in the computer's hard drive. The size of the image is 32 MB and consecutive images can be saved approximately in 1-s intervals.

Fig. 3 shows the screen captures for four different image display modes. The name of the software is HyperGrab shown on the very top of the blue bar. The control buttons are located on the left side of the display. Because the menu buttons are not legible on Fig. 3, the button names are typed in Fig. 3a. The Not Live button can be toggled between Live and Not Live to show the last captured images or live images. The default display shows the four black-and-white band images in scaled gray levels and pixel resolution (Fig. 3a). Although the images are captured in 12 bits with 2048 by 2048 pixels, they are scaled to 8 bits and resampled to 512 by 512 pixels for display. The CIR button allows the CIR composite to be viewed on the NIR quadrant of the display (Fig. 3b), while the Color button allows the normal color composite to be viewed on the red band quadrant. However, only either the CIR or a color composite can be shown along with three other band images. Any single band image, CIR composite or color composite can be viewed with 1024 by 1024 pixels by simply clicking the band image or composite on the display. The color composite and the CIR composite of the band images are shown in Figs. 3c and 3d, respectively.

## 2.3. Image Alignment

As discussed previously, one problem associated with this type of multispectral imaging systems is the misalignment among the band images. The adjustable mounts attached to the cameras are used to align the cameras so that they cover approximately the same field of view. Since the airborne imaging system can be flown at various altitudes from hundreds to thousands of meters, it is

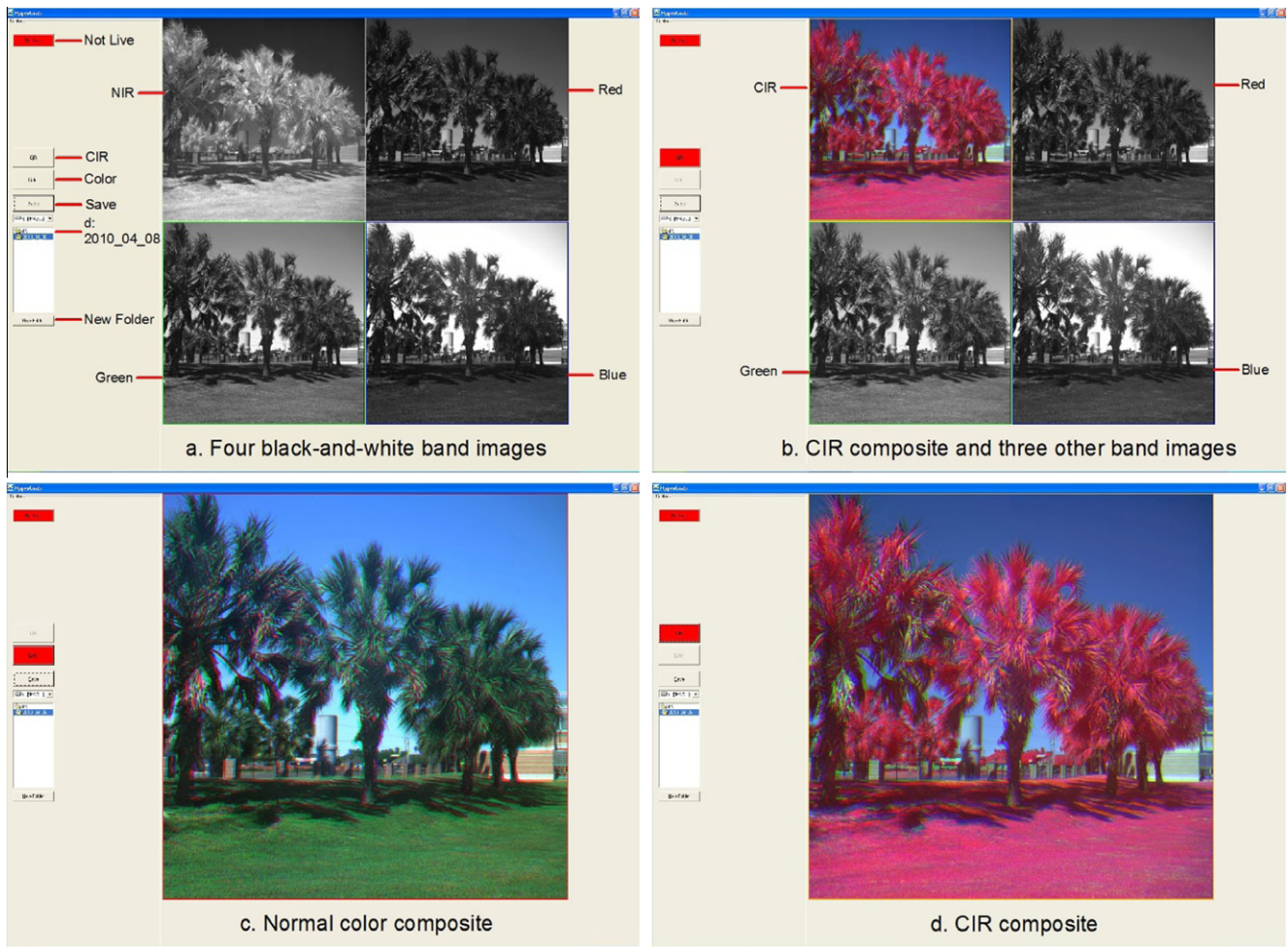


Fig. 3. Screen captures of four different image display modes. Because the menu buttons are not legible, the button names are typed on the screen capture in Fig. 3a.

impossible to align the cameras for all the flight altitudes. To obtain appropriate alignment, the cameras were positioned horizontally to view the trees, grass, buildings and other objects through a window of a USDA-ARS Remote Sensing building at Weslaco, Texas. The cameras were then aligned by viewing a water tower that is approximately 2000 m away. After the alignment, the water tower is located in the same area on each band image and the color and CIR composites images are used to verify the alignment. Once aligned, the system can be used for image acquisition at various altitudes. However, it is always necessary to check the alignment before image acquisition because the alignment can be changed by the vibrations on the aircraft or when the system is transported.

The color and CIR images shown in Fig. 3 indicate that the band images appear to be aligned. However, when the full images are viewed on the computer screen, the misalignment among the band images can be clearly seen, especially for the trees that are close to the cameras. Although the mechanical alignment ensures that the four cameras capture images with maximum overlapping areas, it is not sufficient for data extraction and image analysis. Therefore, first- and second-order polynomial transformation models can be used to more accurately align the band images. A first-order transformation is a linear transformation with the following form:

$$\begin{cases} x_o = a_1 + a_2x_i + a_3y_i \\ y_o = b_1 + b_2x_i + b_3y_i \end{cases} \quad (1)$$

where  $x_i$  and  $y_i$  are the coordinates in a raw band image (input);  $x_o$  and  $y_o$  are the registered or aligned coordinates (output);  $a_1$ ,  $a_2$ , and  $a_3$  are the coefficients of the transformation in the  $x$  direction; and  $b_1$ ,  $b_2$ , and  $b_3$  are the coefficients of the transformation in the  $y$  direction.

A linear transformation will shift, scale and rotate the raw band image to align with a reference band image. For the four band images, one band (i.e., the red band) can be selected as the reference band image and the other three bands will be registered to it. There will be a different transformation model for each of the three band images. To determine the transformation coefficients, at least three reference points are required. In practice, many more points are used to increase the accuracy of the transformation. Thus the least squares method can be used to estimate the coefficients.

Let the number of reference points be  $n$ . The coordinates for the reference points on the reference band image are  $(x_{o1}, y_{o1}), (x_{o2}, y_{o2}), \dots, (x_{on}, y_{on})$  and the coordinates for the corresponding points on the input band images are  $(x_{i1}, y_{i1}), (x_{i2}, y_{i2}), \dots, (x_{in}, y_{in})$ . The least squares estimates of the transformation coefficients are as follows:

$$\begin{cases} A = (C^T C)^{-1} (C^T X_o) \\ B = (C^T C)^{-1} (C^T Y_o) \end{cases} \quad (2)$$

where

$$A = \begin{bmatrix} a_1 \\ a_2 \\ a_3 \end{bmatrix}, \quad B = \begin{bmatrix} b_1 \\ b_2 \\ b_3 \end{bmatrix}, \quad X_o = \begin{bmatrix} x_{o1} \\ x_{o2} \\ \vdots \\ x_{on} \end{bmatrix}, \quad Y_o = \begin{bmatrix} y_{o1} \\ y_{o2} \\ \vdots \\ y_{on} \end{bmatrix}, \quad \text{and}$$

$$C = \begin{bmatrix} 1 & x_{i1} & y_{i1} \\ 1 & x_{i2} & y_{i2} \\ \vdots & \vdots & \vdots \\ 1 & x_{in} & y_{in} \end{bmatrix}.$$

Eq. (2) can be used to transform the input raw band image to geometrically match the reference band image. Unless only three points are used, there will not be a perfect fit for the  $n$  reference points. To measure the accuracy of the transformed image, an inverse transformation is performed to transform the reference coordinates back to the coordinates in the input image. For any reference point  $(x_o, y_o)$ , its retransformed point  $(x_r, y_r)$  in the input image can be derived from Eq. (1) by replacing  $(x_i, y_i)$  with  $(x_r, y_r)$ , that is,

$$\begin{bmatrix} x_r \\ y_r \end{bmatrix} = \begin{bmatrix} a_2 & a_3 \\ b_2 & b_3 \end{bmatrix}^{-1} \begin{bmatrix} x_o - a_1 \\ y_o - b_1 \end{bmatrix} \quad (3)$$

The difference between the input  $x$ -coordinate,  $x_i$ , and the retransformed  $x$ -coordinate,  $x_r$ , is the  $x$  residual,  $XR$ , and the difference between the input  $y$ -coordinate,  $y_i$ , and the retransformed  $y$ -coordinate,  $y_r$ , is the  $y$  residual,  $YR$ . The root mean square (RMS) error is the distance between the input point and the retransformed point in the input image coordinate system. The RMS error,  $R$ , for any reference point is calculated with a distance formula:

$$R = \sqrt{(x_r - x_i)^2 + (y_r - y_i)^2} = \sqrt{XR^2 + YR^2} \quad (4)$$

For the  $n$  reference points, the  $x$  RMS error,  $R_x$ , the  $y$  RMS error,  $R_y$ , and the total RMS error,  $R_t$ , are calculated as follows:

$$R_x = \sqrt{\frac{1}{n} \sum_{j=1}^n XR_j^2}, \quad R_y = \sqrt{\frac{1}{n} \sum_{j=1}^n YR_j^2}, \quad \text{and} \quad R_t = \sqrt{R_x^2 + R_y^2} \quad (5)$$

RMS errors indicate how good the alignment is between the input band and the reference band. The smaller the RMS errors, the better the alignment is. A RMS error of 2 indicates the retransformed pixel can be 2 pixels away from the input pixel. Although a higher order transformation can be used to reduce the RMS errors, more reference points are needed for the calculation. Generally, the first order transformation should be sufficient for band to band alignment since the relative distortion between the band images is small. However, if the RMS errors exceed the error tolerance for a particular application, a second order transformation can be used. Then three second-order terms will be added to Eq. (1) and at least six reference points are required to calculate the transformation coefficients. Although Eqs. (1)–(5) can be implemented using a spreadsheet such as Microsoft Excel or a C++ program, most image processing software can be used to perform this procedure.

After the coordinate transformation, pixels are moved to new locations and the values of the pixels need to be assigned. Since the input image and the reference image have the same pixel array, the original pixel values can be assigned to the corresponding new pixels. However, because of small differences in the CCD sensors and orientations of the cameras in the aluminum frame, the transformed input image may not match the reference image pixel by pixel. Therefore, a resampling procedure is needed to assign pixel values for the aligned image. Although several resampling methods are available, the nearest neighbor algorithm is more appropriate for this purpose because it simply assigns the value of the closest pixel in the input image to the new pixel and it does not change

the original data values. If necessary, when the aligned image is to be rectified to a map coordinate system, other resampling methods such as bilinear interpolation and cubic convolution can be used to achieve data smoothing and other effects.

#### 2.4. Ground coverage and pixel size

The ground coverage of the imaging system can be determined by the following formula:

$$G = \frac{S}{F}H \quad (6)$$

where  $G$  is the ground coverage (m);  $S$  is the side of the square sensor (15.2 mm);  $F$  is the focal length of the lens (24 mm), and  $H$  is the flight height above the ground (m). Thus Eq. (6) can be simply written as

$$G = \frac{19}{30}H = 0.633H \quad (7)$$

The pixel size of the image can be determined by the following formula:

$$P = \frac{19B}{61440}H = 3.09 \times 10^{-4}H \quad (8)$$

where  $P$  is ground pixel size (m) and  $B$  is the binning factor. A binning factor of 2 in both horizontal and vertical directions will reduce the image array to  $1024 \times 1024$  pixels. Table 2 gives ground coverage and pixel size of the multispectral imaging system at commonly-used flight heights and two binning factors. Since flight height is normally adjusted in 500 ft (152 m) or 1000 ft (305 m) increments in the US, the information listed in this table can be used for quick reference in determining appropriate flight height based on pixel size and ground coverage requirements.

#### 2.5. Image acquisition

A Cessna 206 single-engine aircraft was used as the platform for airborne image acquisition testing. The multispectral system and the hyperspectral system were aligned and installed in the aircraft via a camera port (Fig. 4). For optimal image quality, each camera was individually focused and the exposure time and aperture were initially set based on the images taken on the ground. Airborne images were then taken from diverse target areas with a wide range of reflectance. The camera parameters were readjusted so that these settings would be valid for different applications without the need to change aperture settings. For example, Fig. 5 shows the histograms for the four band images acquired from an area with diverse ground targets ranging from dark asphalt roads, water

**Table 2**  
Ground coverage and pixel size of the multispectral imaging system at different flight heights and two binning factors.

Flight height		Ground coverage (m)	Pixel size (m)	
(ft)	(m)		Binning = 1	Binning = 2
1000	305	193	0.094	0.189
2000	610	386	0.189	0.377
3000	914	579	0.283	0.566
4000	1219	772	0.377	0.754
5000	1524	965	0.471	0.943
6000	1829	1158	0.566	1.131
7000	2134	1351	0.66	1.32
8000	2438	1544	0.754	1.508
9000	2743	1737	0.848	1.697
10,000	3048	1930	0.943	1.885
11,000	3353	2123	1.037	2.074
12,000	3658	2316	1.131	2.262

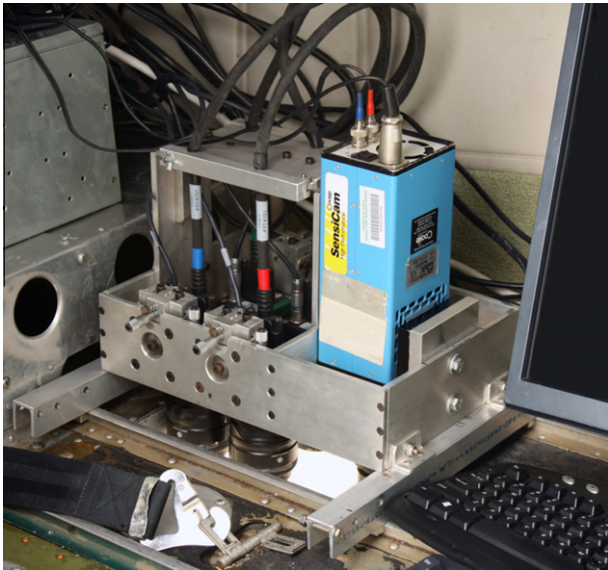


**Fig. 4.** A four-camera imaging system along with a hyperspectral camera (blue color) installed over a camera port in a Cessna 206 aircraft. (For interpretation of the references to colour in this figure legend, the reader is referred to the web version of this article.)

bodies, to healthy plants and highly reflective building roofs. The histograms of the bands are well spread within the dynamic range without saturation, indicating the cameras were properly adjusted. For airborne testing of the system, full resolution images were obtained under sunny and calm conditions from agricultural fields, rangelands, and waterways in south Texas. Images were taken in altitudes ranging from 610 m (2000 ft) to 3050 m (10,000 ft).

Airborne hyperspectral imagery was taken simultaneously along with airborne multispectral imagery from some study sites during the image acquisition testing. The hyperspectral imagery has the potential for identifying optimal narrow bands or combinations of bands for some applications. If the identified bands are more suitable than the general-purpose bands, the four cameras can then be filtered with the selected bands for particular applications. The acquired hyperspectral imagery was not used in this paper.

### 3. Application examples

Five application examples are presented in this section to illustrate the use of the multispectral imaging system for monitoring crop conditions, mapping invasive weeds, and assessing wetland conditions. The cameras were equipped with four 40-nm bandwidth filters with center wavelengths of 480 nm (blue), 560 nm (green), 650 nm (red), and 830 nm (NIR) for these applications. The exposure time was set at 8.632 ms for all the cameras. The aperture was set at  $f/5.6$  for the NIR band,  $f/8.4$  for the blue and red bands, and  $f/11$  for the green band. The apertures for the cameras were so selected that the histograms of the images from diverse target areas were well spread within the dynamic range without saturation. All the images were aligned using the procedure described above. ERDAS Imagine (ERDAS, Inc., Norcross, GA) was used to perform the alignment. The red band image was selected as the reference image and the other three band images were registered to the red band image. Further image processing and analysis will be performed in separate studies.

#### 3.1. Mapping cotton root rot

Cotton root rot, also known as *Phymatotrichum* root rot, is caused by the soilborne fungus *Phymatotrichopsis omnivora*. The

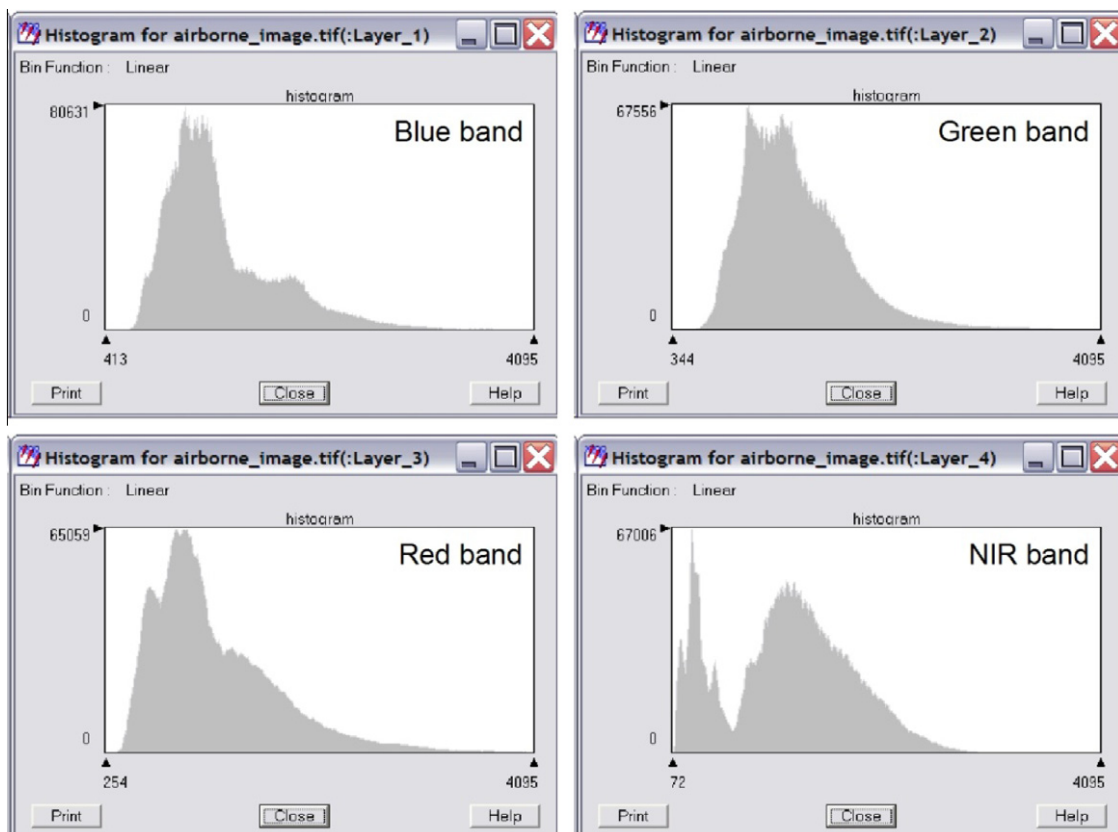


**Fig. 5.** Histograms for the four band images acquired with a four-camera imaging system from an area with diverse ground cover types in south Texas.

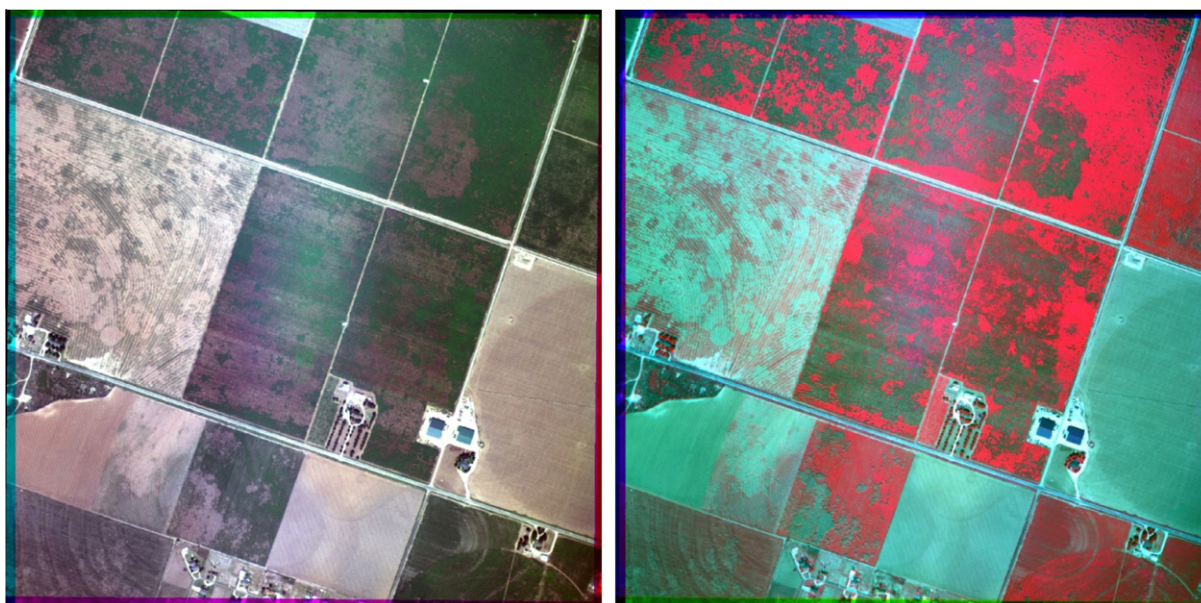


Fig. 6. Color composite (left) and CIR composite of an aligned four-band image acquired on September 25, 2009, from a root rot-infected area near San Angelo, Texas.

Table 3

Root mean square (RMS) errors for registering blue, green and NIR band images to the red band image using the first order transformation based on 4 to 20 reference points for a four-band image acquired from a cotton root rot-infected area.

Reference points	Blue band			Green band			NIR band		
	x	y	Total	x	y	Total	x	y	Total
4	0.2	0.3	0.4	0	0.1	0.1	0.3	0.3	0.5
5	0.3	0.3	0.5	0.1	0.2	0.2	0.3	0.3	0.5
6	0.4	0.4	0.5	0.1	0.2	0.2	0.4	0.5	0.6
7	0.4	0.6	0.7	0.1	0.2	0.2	0.6	0.5	0.8
8	0.4	0.6	0.7	0.2	0.2	0.3	0.6	0.5	0.8
9	0.5	0.6	0.8	0.2	0.2	0.3	0.6	0.5	0.8
10	0.5	0.6	0.8	0.2	0.2	0.3	0.7	0.5	0.8
11	0.5	0.6	0.8	0.2	0.2	0.3	0.6	0.6	0.9
12	0.5	0.7	0.8	0.2	0.2	0.3	0.8	0.8	1.1
13	0.5	0.6	0.8	0.2	0.2	0.3	0.8	0.7	1.1
14	0.5	0.6	0.8	0.2	0.2	0.3	0.8	0.7	1.1
15	0.5	0.6	0.8	0.2	0.2	0.3	0.8	0.7	1.1
16	0.6	0.6	0.8	0.2	0.3	0.4	0.8	0.7	1.1
17	0.5	0.6	0.8	0.3	0.3	0.4	0.8	0.7	1.1
18	0.6	0.6	0.8	0.2	0.3	0.4	0.8	0.7	1.1
19	0.6	0.6	0.8	0.3	0.3	0.4	0.8	0.7	1.1
20	0.6	0.6	0.8	0.3	0.3	0.4	0.8	0.6	1

fungus is prevalent in calcareous, alkaline clay loam soils and in areas with high summer temperatures and moist conditions (Smith et al., 1962). Cotton root rot is a major cotton disease affecting cotton production in the southwestern and south central US. Accurate delineation of root rot infestations is necessary for cost-effective management of the disease. The full extent of root rot damage within cotton fields is usually not apparent at ground level, and any attempt to delineate or map root rot areas on the ground is a challenge. Remote sensing would, however, provide a convenient and useful means of recording the extent of crop damage by detecting changes in the plant canopy. With recent advances in remote sensing, global positioning systems (GPS), and image processing techniques, this disease can be more effectively detected and mapped for management.

Fig. 6 shows the color and CIR composite images of an aligned four-band image acquired on September 27, 2010, from a root rot-infected area near San Angelo, Texas. The image was taken at an altitude of 2438 m (8000 ft) with a ground pixel resolution of

0.75 m. The cotton fields on the image were severely infected with cotton root rot. On the color image, healthy cotton plants have a dark green color, when infected plants have a grayish color similar to bare soil. On the CIR image, healthy plants have a reddish-magenta tone, while infected plants have a cyan or greenish color. In fact, the image was taken shortly before harvest and the most of infected plants were dead. Although root rot-infected areas can be easily separated from the non-infected areas on both images, the CIR image appears to be more effective because of the high NIR reflectance for healthy plants. The image can be used to quantify infected areas within the fields for the management and control of the disease. Temporal images acquired within and across growing seasons can be used to monitor the progression of the disease.

The different color shades along the four sides of the images are due to the misalignment among the bands. Table 3 gives the RMS errors for registering the blue, green and NIR band images to the red band image using the first-order transformation when 4 to 20 reference points were used. As the number of reference points increased, the RMS errors increased and then stabilized for each band. It appears that 8–12 reference points evenly distributed within the image will be sufficient for band-to-band alignment. The total RMS error was 0.8 pixels for the blue band, 0.4 pixels for the red band and 1.1 pixels for the NIR band when 12 reference points were used. These errors are acceptable for mapping root rot infections and most other agricultural applications. If smaller RMS errors are necessary, the second order transformation can be used. Table 4 gives the RMS errors using the second-order transformation when 7–20 reference points were used. The second-order transformation generally lowered RMS errors, especially for the NIR band image.

Yang et al. (2012) used airborne multispectral imagery from the four-camera system for detecting and monitoring the expansion of root rot infection in cotton fields within and across growing seasons. Airborne multispectral imagery was taken from dozens of infected fields in central and south Texas multiple times during the growing seasons in 2010 and 2011. The images were successfully used to quantify the infection and its progression within the growing seasons and the consistency and change across different growing seasons. This information will be useful for the understanding of the progression of the disease and for the development of site-specific treatment plans for the disease.

**Table 4**

Root mean square (RMS) errors for registering blue, green and NIR band images to the red band image using the second order transformation based on 7–20 reference points for a four-band image acquired from a cotton root rot-infected area.

Reference points	Blue band			Green band			NIR band		
	x	y	Total	x	y	Total	x	y	Total
7	0	0.1	0.2	0.1	0	0.1	0	0	0.2
8	0	0.2	0.2	0.1	0	0.2	0	0	0.3
9	0	0.2	0.2	0.1	0	0.2	0	0	0.4
10	0	0.3	0.4	0.1	0	0.2	0	0	0.4
11	0	0.3	0.4	0.1	0	0.2	0	0	0.5
12	0	0.3	0.5	0.1	0	0.2	0	0	0.5
13	0	0.3	0.4	0.1	0	0.2	0	0	0.5
14	0	0.3	0.5	0.2	0	0.3	0	0	0.5
15	0	0.3	0.5	0.2	0	0.3	0	0	0.5
16	0	0.3	0.5	0.2	0	0.4	0	0	0.5
17	0	0.3	0.5	0.2	0	0.4	0	0	0.5
18	0	0.3	0.5	0.2	0	0.4	0	0	0.5
19	0	0.3	0.5	0.3	0	0.4	0	0	0.5
20	0	0.3	0.5	0.2	0	0.4	0	0	0.5

### 3.2. Monitoring citrus groves

Fig. 7 shows the color and CIR composite images of an aligned four-band image acquired on March 2, 2010, from a citrus growing area in Weslaco, Texas. The image was taken at an altitude of 1524 m (5000 ft) with a ground pixel resolution of 0.47 m. These images clearly show the citrus groves and their general growing conditions in the imaging area. Healthy and large trees have a dark green color in the color image and a red color on the CIR image. Individual trees can be clearly identified and their diameters can be measured when the image is zoomed in on a computer screen. The locations of missing trees within the groves are clearly visible.

The image also reveals problematic groves or trees that are affected by pests or soil problems. For example, some of the trees in the square grove near the upper left side didn't look healthy because of their slightly smaller size and dark reddish tone on the CIR image. Ground observations verified that some of the trees near the center of the grove were infected with greasy spot, a common citrus foliar disease caused by the fungus *Mycosphaerella citri* Whiteside (Whiteside, 1974). Infected trees have leaves decaying with yellow and dark spots, and eventually are defoliated. Greasy spot reduces tree vigor and results in yield loss and low fruit

quality. Another rectangular grove at the lower portion of image had large soil background exposure and a large number of missing trees or stunted trees. This grove is located in a low area with heavy clay soil, making it difficult for tree roots to grow. The conditions in other groves can also be visually assessed from the images initially and followed by ground surveys to identify the particular problems.

Table 5 gives the total RMS errors for registering the blue, green and NIR band images to the red band image using the first-order transformation when 4 to 20 reference points were used for the citrus groves. The total RMS error was 1.8 pixels for the blue band, 0.7 pixels for the green band and 1.1 pixels for the NIR band when 12 reference points were used. The total RMS errors for the other three application examples (giant reed, saltcedar and mangrove) are also summarized in the table. The total RMS errors are within one pixel for most of the cases and between 1 and 2 pixels for the rest. Table 6 summarizes the total RMS errors for registering the blue, green and NIR band images to the red band image using the second-order transformation when 7–20 reference points were used for the citrus groves and the other three examples. Clearly, the second-order transformation generally lowered RMS errors and the total RMS errors were all within one pixel.

### 3.3. Mapping giant reed

Giant reed (*Arundo donax* L.) is a bamboo-like perennial grass that grows 3 to 10 meters tall and spreads from horizontal rootstocks below the soil to form large colonies (Dudley, 2000). It typically grows in riparian areas and floodplains and can be found on wet stream banks, gravel bars, or dry banks away from permanent water. Today giant reed is an invasive weed throughout the southern half of the United States and northern Mexico with the densest stands growing along the coastal rivers of southern California and the Rio Grande in Texas (Bell, 1997; Everitt et al., 2004; Yang et al., 2011). Giant reed consumes excessive amounts of water to supply its incredible rate of growth and it displaces native vegetation, leading to the destruction of wildlife habitats.

Accurate information on the spatial distribution and infested areas of giant reed is essential for effective management of this invasive weed. Remote sensing has the potential for providing timely and accurate information on the infestations of giant reed.

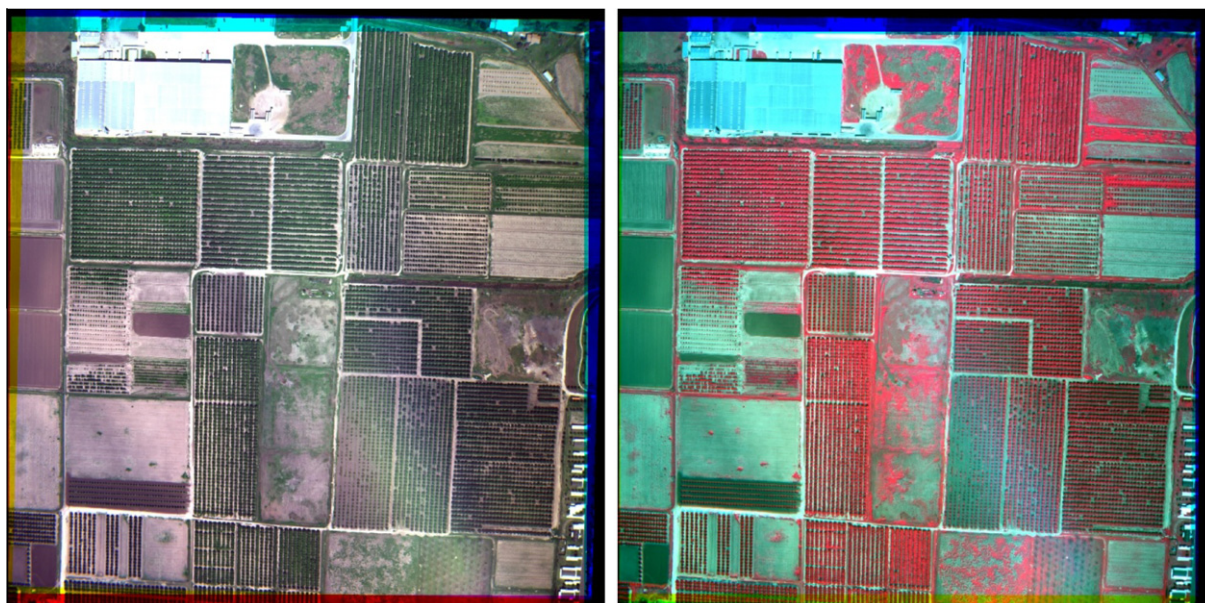


Fig. 7. Color composite (left) and CIR composite of an aligned four-band image acquired on March 2, 2010, from a citrus growing area in Weslaco, Texas.

**Table 5**

Total root mean square (RMS) errors for registering blue, green and NIR band images to the red band image using the first order transformation based on 4–20 reference points for four-band images acquired from citrus groves, a giant reed-infested site, a saltcedar-infested site, and a mangrove wetland area.

Reference points	Citrus			Giant reed			Saltcedar			Mangrove		
	Blue	Green	NIR	Blue	Green	NIR	Blue	Green	NIR	Blue	Green	NIR
4	1.6	0.5	1	0.5	0.3	1.6	0.2	0.8	0.7	1.6	0.4	0.6
5	1.6	0.5	1	0.5	0.6	1.5	0.3	0.7	0.8	1.6	0.4	0.6
6	1.7	0.5	1.1	0.6	0.6	1.5	0.4	0.7	0.7	1.7	0.5	0.8
7	1.8	0.6	1.2	0.6	0.6	1.5	0.4	0.7	0.7	1.8	0.4	0.8
8	1.8	0.6	1.2	0.6	0.6	1.6	0.4	0.7	0.7	1.8	0.5	0.8
9	1.7	0.6	1.1	0.6	0.5	1.6	0.4	0.7	0.8	1.7	0.5	1
10	1.7	0.6	1.1	0.6	0.5	1.5	0.3	0.7	0.7	1.7	0.5	1
11	1.7	0.6	1.1	0.6	0.5	1.5	0.4	0.6	0.8	1.7	0.5	1
12	1.8	0.7	1.1	0.6	0.5	1.5	0.4	0.6	0.7	1.8	0.5	1
13	1.8	0.7	1.2	0.5	0.5	1.4	0.4	0.6	0.7	1.8	0.5	1
14	1.7	0.7	1.3	0.6	0.5	1.4	0.4	0.6	0.7	1.7	0.5	1
15	1.7	0.7	1.2	0.6	0.5	1.4	0.4	0.7	0.8	1.7	0.5	1
16	1.7	0.7	1.3	0.6	0.5	1.5	0.4	0.7	0.7	1.7	0.5	1.1
17	1.6	0.7	1.2	0.6	0.5	1.5	0.4	0.8	0.8	1.6	0.5	1.1
18	1.6	0.7	1.2	0.6	0.5	1.4	0.4	0.8	0.8	1.6	0.5	1
19	1.6	0.6	1.2	0.6	0.5	1.4	0.4	0.8	0.8	1.6	0.5	1
20	1.5	0.6	1.2	0.6	0.5	1.4	0.4	0.8	0.8	1.5	0.5	1

**Table 6**

Total root mean square (RMS) errors for registering blue, green and NIR band images to the red band image using the second order transformation based on 7 to 20 reference points for four-band images acquired from citrus groves, a giant reed-infested site, a saltcedar-infested site, and a mangrove wetland area.

Reference points	Citrus			Giant reed			Saltcedar			Mangrove		
	Blue	Green	NIR	Blue	Green	NIR	Blue	Green	NIR	Blue	Green	NIR
7	0	0.1	0.1	0.1	0.2	0.2	0.2	0.1	0	0	0.1	0.1
8	0.2	0.1	0.3	0.1	0.3	0.3	0.2	0.2	0.3	0.2	0.2	0.5
9	0.3	0.2	0.5	0.2	0.3	0.3	0.2	0.3	0.4	0.3	0.2	0.8
10	0.3	0.3	0.7	0.2	0.3	0.3	0.2	0.3	0.4	0.3	0.2	0.9
11	0.2	0.4	0.8	0.2	0.4	0.4	0.2	0.3	0.4	0.2	0.2	0.8
12	0.2	0.4	0.7	0.2	0.4	0.6	0.2	0.3	0.4	0.2	0.2	0.8
13	0.2	0.5	0.8	0.2	0.4	0.6	0.2	0.4	0.5	0.2	0.3	0.8
14	0.2	0.5	0.8	0.2	0.4	0.6	0.2	0.4	0.5	0.2	0.3	0.8
15	0.3	0.5	0.8	0.3	0.4	0.7	0.2	0.4	0.5	0.3	0.3	0.8
16	0.3	0.5	0.9	0.3	0.4	0.6	0.3	0.4	0.5	0.3	0.3	0.8
17	0.2	0.5	0.9	0.3	0.4	0.6	0.3	0.4	0.5	0.2	0.3	0.8
18	0.3	0.5	0.9	0.3	0.4	0.6	0.3	0.4	0.5	0.3	0.3	0.8
19	0.3	0.5	0.9	0.3	0.4	0.6	0.3	0.4	0.5	0.3	0.3	0.7
20	0.3	0.5	0.8	0.3	0.4	0.6	0.3	0.4	0.5	0.3	0.3	0.7

Fig. 8 shows the color and CIR composites of an aligned four-band image acquired on October 8, 2010, from a giant reed-infested area near Quemado, Texas. The image was taken at an altitude of 2896 m (9500 ft) with a ground pixel resolution of 0.89 m. On the normal color image, giant reed has a light green color, while mixed woody species have dark green or brownish tone. On the CIR image, giant reed shows a bright reddish tone, while mixed woody species have a dark red response.

### 3.4. Mapping Saltcedar

Saltcedar (*Tamarix* spp.) is a perennial shrub or tree that was introduced to the US from Europe and Asia in 1800s for ornamental use and erosion prevention (Baum, 1967). Several species of saltcedar are invaders of riparian sites in the southwestern US and northern Mexico. They form dense, low thickets that displace native plant communities, degrade wildlife habitat, increase soil salinity and wildfires, reduce water available for agriculture and municipalities, and reduce recreational use of affected areas (Deloach et al., 2003). Saltcedar communities are also much less valuable for wildlife than the native riparian communities they displace.

One of the important tasks for effective control of saltcedar is to map its distribution and quantify the infested areas. Remote sensing has the potential for this purpose. Fig. 9 shows the color and

CIR composites of an aligned four-band image acquired on November 4, 2009, from a saltcedar-infested area in Candelaria, Texas. The image was taken at an altitude of 3048 m (10,000 ft) with a ground pixel resolution of 0.94 m. Saltcedar has a dark green to yellow green color on the normal color image and a reddish color on the CIR image. Mixed brush species (senesced) toward the west edge of the imaging area have a brownish color on the color image and a greenish tone on the CIR image.

### 3.5. Monitoring mangrove wetland

Mangrove wetlands are regarded as economically and ecologically important ecosystems due to their intermediate position between the marine and terrestrial environments. They have high productivity of litter fall and woody biomass, provide habitat and detritus food for fish and shellfish, and function as nurseries for a variety of fishes, prawns and shellfishes (Day et al., 1996). Moreover, mangrove forests provide a natural barrier that helps to prevent shoreline erosion, shielding inland areas from severe damage during hurricanes and tidal waves (Marshall, 1994). Efforts are needed to protect and restore these valuable ecosystems. To formulate effective management and conservation plans and practices, it is very important to understand the compositions and distributions of plant communities in mangrove wetlands. Because of their inaccessibility and large extent, remote sensing can provide a

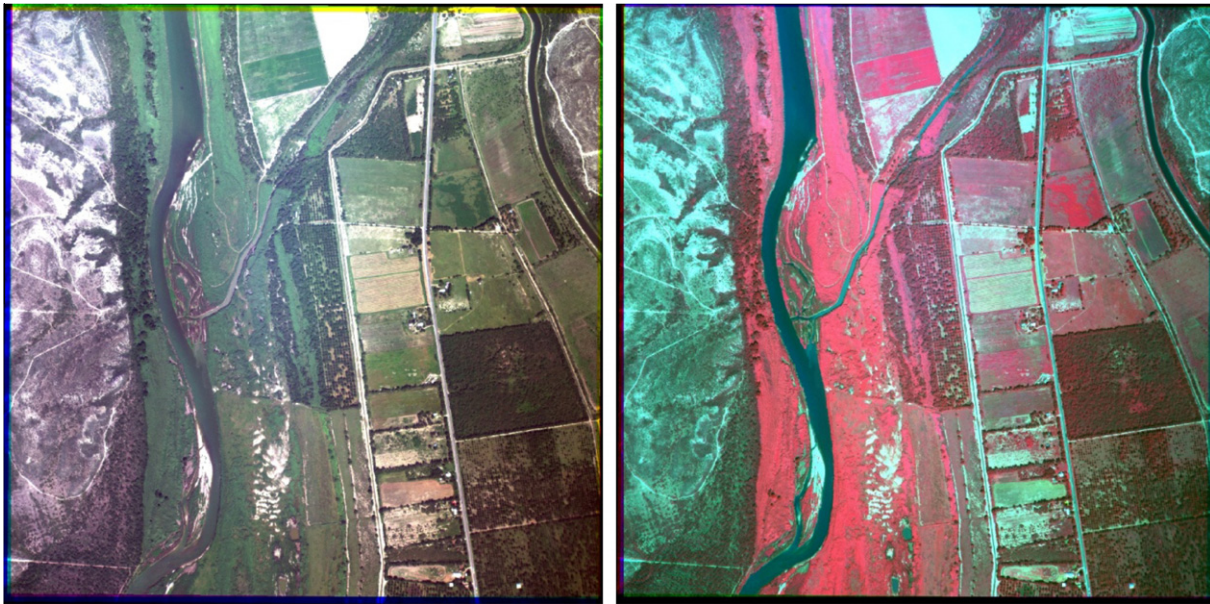


Fig. 8. Color composite (left) and CIR composite of an aligned four-band image acquired on October 8, 2010, from a giant reed-infested area near Quemado, Texas.

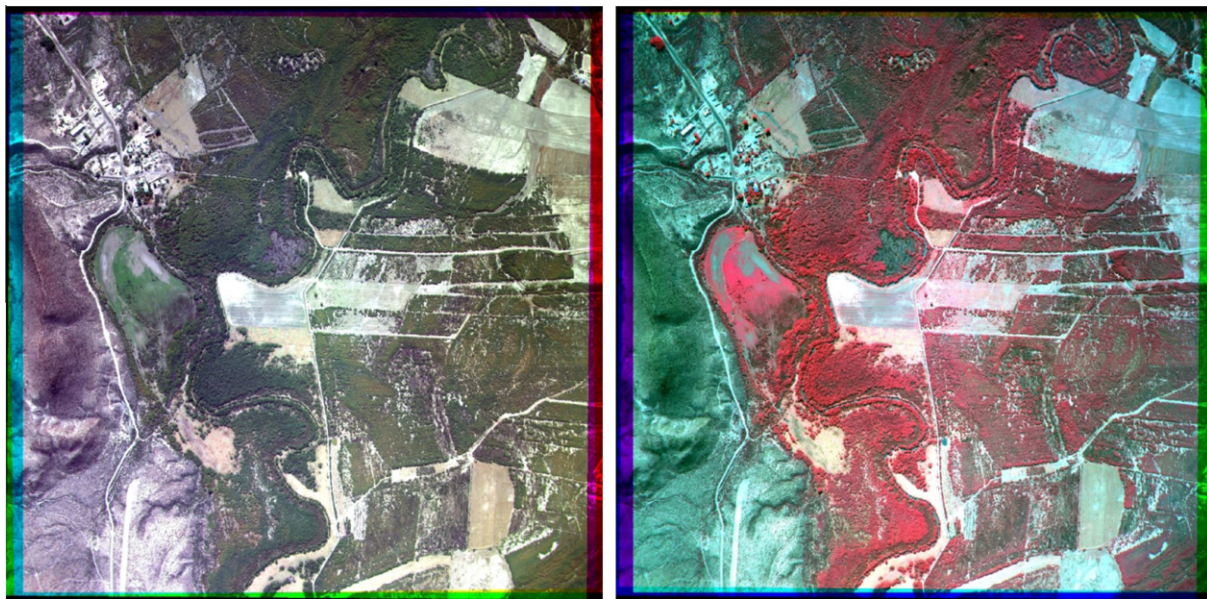


Fig. 9. Color composite (left) and CIR composite of an aligned four-band image acquired on November 4, 2009, from a saltcedar-infested area in Candelaria, Texas.

cost-effective tool to monitor and map the distribution and dynamics of these plant communities.

Fig. 10 shows the color and CIR composites of an aligned four-band image acquired on March 1, 2010, from a black mangrove [*Avicennia germinans* (L.) L.] wetland area in South Padre Island, Texas. The image was taken at an altitude of 1219 m (4000 ft) with a ground pixel resolution of 0.38 m. Black mangrove trees in this area are 1.5–2 m tall. They generally grow along the west coast of the island with strips ranging from a few meters to over 200 m wide. Black mangrove has a dark green color on the color image and a dark reddish tone on the CIR image. The grass growing between the roads looks lime green on the color image and bright red on the CIR image. The murky water on the west side has a grayish to bluish color on the color image and a greenish to bluish tone on the CIR image.

#### 4. Conclusions

An airborne four-camera multispectral imaging system was designed, assembled, and tested in this study. The system met all the design requirements. It can acquire 12-bit digital images with  $2048 \times 2048$  pixels in four spectral bands in the 400–900 nm spectral range. The camera parameters were optimized to acquire images in the blue (430–470 nm), green (530–570 nm), red (630–670 nm), and NIR (810–850 nm) bands, allowing both normal color and CIR images to be obtained simultaneously. Moreover, the cameras can be fitted with different filters to implement the optimal bands identified by a hyperspectral system or other band combinations for particular applications. The wide radiometric range of the cameras allows images to be taken from diverse target areas without the need to change aperture settings. The adjustable

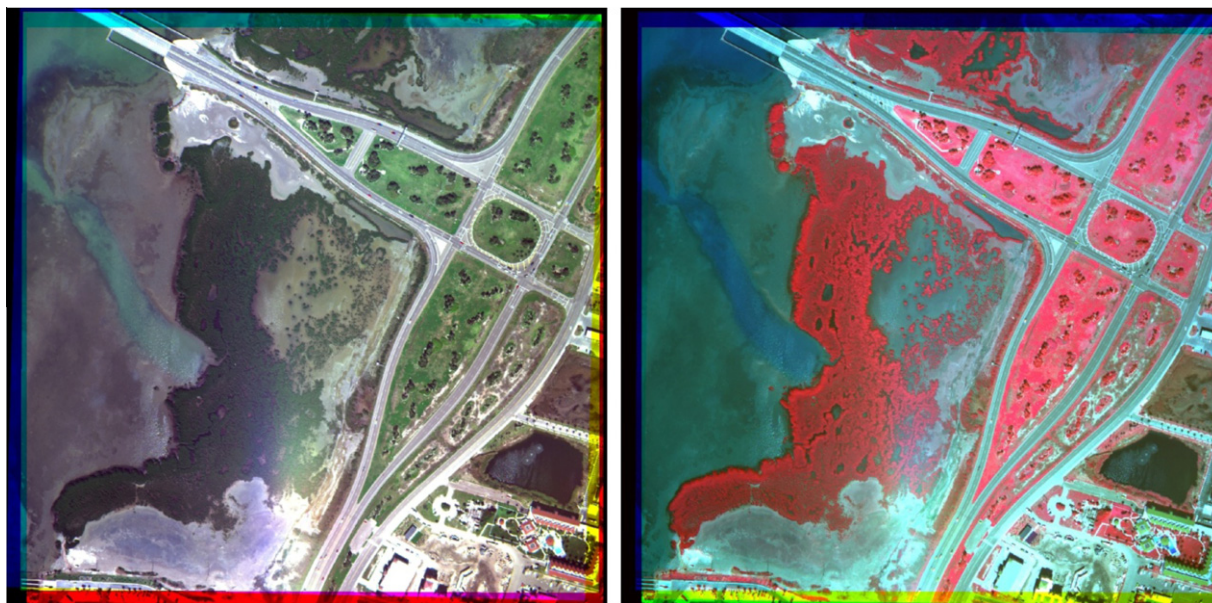


Fig. 10. Color composite (left) and CIR composite of an aligned four-band image acquired on March 1, 2010, from a mangrove wetland area in South Padre Island, Texas.

mounts attached to the cameras ensure the cameras to have a similar field of view and allow aligned color and CIR composite images to be viewed for real-time assessment during the flight. First- and second-order transformations can be used to further align the four band images for image processing and analysis. The RMS errors among the bands are generally within two pixels based on 10–12 reference points with the first-order transformation and within one pixel based 12–15 points with the second-order transformation. Both ground and airborne experiments showed that the system performed well and was reliable. The images acquired from a root rot-infected area, citrus groves, a giant reed-infested site, a saltcedar-infested site, and a mangrove wetland area demonstrated that imagery from this high resolution four-camera imaging system can be used for monitoring crop pest and growing conditions, mapping invasive weeds, and assessing wetland ecosystems. More experiments will be conducted to evaluate the multispectral imaging system for other remote sensing applications.

### Acknowledgements

The author wishes to thank Bill Mount of Subtechnique, Inc. in Alexandria, VA, for his assistance in assembling the imaging system; Daryl Hill of USDA-APHIS in Mission, TX, and Fred Gomez of USDA-ARS in Weslaco, TX, for test-flying the system and acquiring the example images for this study; and Jim Forward of USDA-ARS in Weslaco, TX, for his assistance in testing the system in the laboratory and in image processing.

### References

- Baum, B.R., 1967. Introduced and naturalized tamarisks in the United States and Canada (Tamaricaceae). *Baileya* 15, 19–25.
- Bell, G.P., 1997. Ecology and management of *Arundo donax* and approaches to riparian habitat restoration in southern California. In: Brock, J.H., Wade, M., Pysek, P., Green, D. (Eds.), *Plant Invasion Studies from North America and Europe*. Blackhuys Publishers, Leiden, The Netherlands, pp. 103–113.
- Day Jr., J.W., Coronado-Molina, C., Vera-Herrera, F.R., Twilley, R., Rivera-Monroy, V.H., Alvarez-Guillen, H., Day, R., Conner, W., 1996. A 7-year record of above-ground net primary production in a southeastern Mexican mangrove forest. *Aquatic Botany* 55, 39–60.
- DeLoach, C.J., Lewis, P.A., Herr, J.C., Carruthers, R.I., Tracy, J.L., Johnson, J., 2003. Host specificity of the leaf beetle, *Diorhabda elongata deserticola* (Coleoptera: Chrysomelidae) from Asia, a biological control agent for saltcedars (Tamarix: Tamaricaceae) in the western United States. *Biological Control* 27, 117–147.
- Dudley, T.L., 2000. *Arundo donax*. In: Bossard, C.C., Randal, J.M., Hosovsky, M.C. (Eds.), *Invasive Plants of California Wildlands*. University of California Press, Berkeley, CA, pp. 53–58.
- Escobar, D.E., Everitt, J.H., Noriega, J.R., Davis, M.R., Cavazos, I., 1997. A true digital imaging system for remote sensing applications. In: *Proceedings of the 16th Biennial Workshop on Color Photography and Videography in Resource Assessment*. American Society for Photogrammetry and Remote Sensing, Bethesda, MD, pp. 470–484.
- Everitt, J.H., Escobar, D.E., Alaniz, M.A., Davis, M.R., 1989. Using multispectral video imagery for detecting soil surface conditions. *Photogrammetric Engineering & Remote Sensing* 55, 467–471.
- Everitt, J.H., Escobar, D.E., Cavazos, I., Noriega, J.R., Davis, M.R., 1995. A three-camera multispectral digital video imaging system. *Remote Sensing of Environment* 54, 333–337.
- Everitt, J.H., Yang, C., Alaniz, M.A., Davis, M.R., Nibling, F.L., DeLoach, C.J., 2004. Canopy spectra of giant reed and associated vegetation. *Journal of Range Management* 57, 561–569.
- Gregory, S., Hedges, P., Elgy, J., 1999. The geometric correction of airborne line-scanner imagery. In: *Proceedings of the 4th International Airborne Remote Sensing Conference and Exhibition/21st Canadian Symposium on Remote Sensing*, vol. 1. ERIM International, Inc., Ann Arbor, MI, pp. 178–185.
- Inman, D., Khosla, R., Reich, R., Westfall, D.G., 2008. Normalized difference vegetation index and soil color-based management zones in irrigated maize. *Agronomy Journal* 100, 60–66.
- King, D.J., 1995. Airborne multispectral digital camera and video sensors: a critical review of systems designs and applications. *Canadian Journal of Remote Sensing* 21, 245–273.
- Kise, M., Park, B., Heitschmidt, G.W., Lawrence, K.C., Windham, W.R., 2010. Multispectral imaging system with interchangeable filter design. *Computers and Electronics in Agriculture* 72 (2), 61–68.
- Lan, Y., Huang, Y., Martin, D.E., Hoffmann, W.C., 2009. Development of an airborne remote sensing system for crop pest management: system integration and verification. *Applied Engineering in Agriculture* 25 (4), 607–615.
- Mao, C., 1999. Hyperspectral imaging systems with digital CCD cameras for both airborne and laboratory application. In: *Proceedings of the 17th Biennial Workshop on Color Photography and Videography in Resource Assessment*. American Society of Photogrammetric Engineering & Remote Sensing, Bethesda, MD, pp. 31–40.
- Marshall, N., 1994. Mangrove conservation in relation to overall environmental consideration. *Hydrobiologia* 285, 303–309.
- Mausel, P.W., Everitt, J.H., Escobar, D.E., King, D.J., 1992. Airborne videography: current status and future perspectives. *Photogrammetric Engineering & Remote Sensing* 58, 1189–1195.
- Meisner, D.E., Lindstrom, O.M., 1985. Design and operation of a color-infrared aerial video system. *Photogrammetric Engineering & Remote Sensing* 51, 555–560.
- Moran, M.S., Inoue, Y., Barnes, E.M., 1997. Opportunities and limitations for image-based remote sensing in precision crop management. *Remote Sensing of Environment* 61, 319–346.
- Nixon, P.R., Escobar, D.E., Menges, R.M., 1985. Use of a multi-band video system for quick assessment of vegetal condition and discrimination of plant species. *Remote Sensing of Environment* 17, 203–208.
- Pearson, R., Mao, C., Grace, J., 1994. Real-time airborne agricultural monitoring. *Remote Sensing of Environment* 49, 304–310.

- Pinter Jr., P.J., Hatfield, J.L., Schepers, J.S., Barnes, E.M., Moran, M.S., Daughtry, C.S.T., Upchurch, D.R., 2003. Remote sensing for crop management. *Photogrammetric Engineering & Remote Sensing* 69 (6), 647–664.
- Senay, G.B., Ward, A.D., Lyon, J.G., Fausey, N.R., Nokes, S.E., 1998. Manipulation of high spatial resolution aircraft remote sensing data for use in site-specific farming. *Transactions of the ASAE* 41 (2), 489–495.
- Smith, H.E., Elliot, F.C., Bird, L.S., 1962. Root Rot Losses of Cotton Can Be Reduced. Publ. No. MP 361. The Texas A&M University System, Texas Agricultural Extension Service, College Station, TX.
- Whiteside, J.O., 1974. Environmental factors affecting infection of citrus leaves by *Mycosphaerella citri*. *Phytopathology* 64, 115–120.
- Yang, C., Anderson, G.L., 1999. Airborne videography to identify spatial plant growth variability for grain sorghum. *Precision Agriculture* 1 (1), 67–79.
- Yang, C., Everitt, J.H., 2007. Evaluating airborne hyperspectral imagery for mapping waterhyacinth infestations. *Journal of Applied Remote Sensing* 1, 013546.
- Yang, C., Everitt, J.H., Davis, M.R., Mao, C., 2003. A CCD camera-based hyperspectral imaging system for stationary and airborne applications. *Geocarto International Journal* 18 (2), 71–80.
- Yang, C., Fernandez, C.J., Everitt, J.H., 2005. Mapping *Phymatotrichum* root rot of cotton using airborne three-band digital imagery. *Transactions of the ASAE* 48 (4), 1619–1626.
- Yang, C., Everitt, J.H., Bradford, J.M., Murden, D., 2009. Comparison of airborne multispectral and hyperspectral imagery for estimating grain sorghum yield. *Transactions of the ASABE* 52 (2), 641–649.
- Yang, C., Everitt, J.H., Goolsby, J.A., 2011. Using aerial photography for mapping giant reed infestations along the Texas–Mexico portion of the Rio Grande. *Invasive Plant Science and Management* 4, 402–410.
- Yang, C., Odvody, G.N., Fernandez, C.J., Landivar, J.A., Minzenmayer, R.R., Nichols, R.L., 2012. Monitoring Cotton root rot progression within and across growing seasons using remote sensing. In: *Proceedings of Beltwide Cotton Conferences*, Memphis, TN, pp. 475–480.